Available online at www.sciencedirect.com
ScienceDirect
Journal of the European Ceramic Society 31 (2011) 273–280
www.elsevier.com/locate/jeurceramsoc

Kinetic study of mullite growth in sanitary-ware production by in situ HT-XRPD. The influence of the filler/flux ratio

Nicoletta Marinoni [a,*], Andrea Pagani [b], Ilaria Adamo [a], Valeria Diella [b], Alessandro Pavese [a,b], Fernando Francescon [c]

[a] *Dipartimento di Scienze della Terra "Ardito Desio", Università degli Studi di Milano, Via Botticelli 23, 20133 Milan, Italy*
[b] *National Research Council, IDPA, Section of Milan, Via Botticelli 23, I-20133 Milan, Italy*
[c] *Ideal Standard International, C.O.E., Ceramic Process Technology, Via Cavassico Inferiore 160, I-32026 Trichiana, BL, Italy*

Received 10 May 2010; received in revised form 20 September 2010; accepted 2 October 2010
Available online 5 November 2010

Abstract

The mullitisation kinetics in a sanitary-ware-like precursor system is here investigated by means of high-temperature X-ray powder diffraction, as a function of the filler/flux ratio. We used a blend based on kaolinite (50 wt%), quartz (10–28 wt%) and Na–feldspar (22–40 wt%). The results show that the content of feldspar boosts the formation of mullite as proven by the apparent activation energy values determined, ranging from 394 to 1111 kJ/mol, and giving a $dE_a/dx_{feldspar} \sim -23$ kJ/mol/wt ($x_{feldspar}$ = feldspar weight fraction). The mullitisation temperature has also been observed to depend on the Na–feldspar content, inasmuch as the sample bearing the smallest amount of feldspar flux exhibits a mullite growth onset between 1100 and 1150 °C, that is at a temperature about 50 °C higher than the one observed in the richer blends. The mullitisation kinetic process is in this work described as a one-mechanism transformation, satisfactorily formalised by Avrami–Erofeyev equation.

Keywords: Mullite; Traditional ceramic; Kinetic analysis; X-ray diffraction

1. Introduction

The understanding of the mechanisms controlling the kinetic of the mullite formation has important implications both for industrial processes, since mullite is a major constituent in a variety of ceramic materials, and for the classification and evolution of high-grade temperature rocks in metamorphic petrogenetic reactions.[1] In the former case, a full knowledge of the mullitisation reaction is a key to design or improve industrial processes for them to yield high mechanical performances final products. The microstructure of a fired body, *i.e.* the spatial distribution of its constituent phases and the interconnections between them, are strictly related to its macroscopic properties, such as total porosity, shrinkage and bending strength.[2,3] In particular, mullite seems to be material to strength enhancement, according to the "mullite hypothesis"[4] that relies upon the interlocking of the fine needle-like crystals[5] characteristic of this phase's habit. Iqbal and Lee[5] pointed out the coexistence of three mullite types showing differences in shape and/or dimension; they use the acronym MI to refer to small (aspect ratio 1–3:1) crystals (primary mullite, supposed from clay relicts), MII and MIII to address to needle-like secondary mullite (related to feldspar melt), with an aspect ratio of 3–10:1 and 30–40:1, respectively.

Many studies have been carried out with the aim of providing models for the mullite growth mechanism, often paying attention to the role of the precursor raw materials,[6–10] and to the differences observed in terms of crystallisation temperature, chemical composition and crystal structure of the resulting mullite. Gualtieri et al.[11] report a study on mullite crystallisation from two kaolinites, thus exploring the influence of the crystallinity degree of the starting phases on the activation energy of the reaction. Tkalcec et al.[8] studied in detail the mullite formation by sol–gel processes. These investigations have provided a basis to discuss diverse models of mullite nucleation and growth.[7,8,11]

The aim of the present work is to investigate by in situ high-temperature X-ray powder diffraction (HT-XRPD) the phase transformations and mullite formation kinetics as a function of the filler/flux ratio, starting from multi-phase precursor

* Corresponding author.
E-mail address: nicoletta.marinoni@unimi.it (N. Marinoni).

0955-2219/$ – see front matter © 2010 Elsevier Ltd. All rights reserved.
doi:10.1016/j.jeurceramsoc.2010.10.002

Table 1
Mineralogical compositions of the samples used for the present study. The temperatures of mullite growth determined in previous experiments have been reported.

	Kaolin (wt%)	Feldspar (wt%)	Quartz (wt%)	Heating ramp (°C/min)	*T* mullite formation (°C)
					Thiswork
Sample *I2*	50	10	40	25	1150
Sample *I3*	50	22	28	25	1100
Sample *I4*	50	40	10	25	1100
Previous studies					
Chen et al.[7]	100			5	1050
Tkalec et al.[8]	#			5	1327*
Gualtieri et al.[11]	100			100	∼1300
Romero et al.[9]	50	10	40	10	985

# Indicates two-phase gels in the system Al_2O_3–SiO_2 as precursor.
* Refers to *T* of mullite growth calculated as an average value on three samples.

systems constituted by kaolinite (clay component), quartz (filler) and feldspar (flux), so as to mimic compositions consistent with those of the industrial practice for sanitary-ware. In such a view, we have explored three filler/flux ratios to shed light on how they affect the mullite's kinetic parameters. In order to simplify the complexity of the system on study, we have chosen to restrict our attention to pure kaolinite instead of a kaolinite-clay blend, commonly used in the industrial practice. To our knowledge, only one kinetic study on the mullite growth in porcelain stoneware has hitherto been performed, by means of thermal analysis.[9]

Preliminary HT-XRPD measurements at equilibrium conditions (from room temperature up to 1200 °C) have been performed with the aim of supplying information on the solid-state reactions occurring in the original mixtures. Then, isothermal kinetic studies, using HT-XRPD, have been carried out to investigate nucleation and growth of mullite by monitoring the time evolution of some diffraction peaks at given temperatures.

2. Sampling

Three different samples (*I2*, *I3*, *I4*) have been prepared by blending quartz, feldspar and kaolinite, as reported in Table 1. Such phases were first suspended in distilled water with deflocculant, and then shaken up for 24 h. Successively, in order to separate the solid powders from the whole, they were centrifuged for 20 min at 4000 rpm and thermally treated at 60 °C for 24 h for drying.

Commercial raw materials, commonly used for the sanitary-ware industrial production, have been employed here; their mineralogical characterisation is discussed by Pagani et al.[12] The laser particle size distributions of the kaolinite, quartz and feldspar samples used for the present study have yielded d_{50}-values of ∼7, 24 and 17 μm, respectively.

3. Experimental

3.1. High-temperature X-ray powder diffraction

The HT-XRPD measurements were collected by means of a Panalytical X'Pert diffractometer, in θ–θ Bragg–Brentano geometry, equipped with a furnace (AHT-PAP1600) that enables achievement of an upper *T* of 1600 °C.[13]

Preliminary HT-XRPD data collections were recorded from room temperature (RT) to 900 °C every 100th °C, and from 900 to 1200 °C every 50th °C, with an heating ramp of 20 °C/min and adopting an equilibration time as long as 3 h at each temperature before starting measurements. These experiments aim at giving general information on (i) the nature of the phases forming upon heating, (ii) their temperature range of crystallisation, and (iii) the most appropriate temperatures to follow the mullite crystallisation by isothermal runs. The XRPD experiments mentioned above were carried out using Cu Kα radiation, exploring the 2θ-angular range of 10–65°, with a step size of 0.03° 2θ and a counting time of 1 s/step. Additional data collections were then performed on the samples after cooling, too. The phase fraction values have been determined using the Rietveld method,[14–16] implemented in the GSAS and EXPGUI software packages,[17,18] adding Al_2O_3-NIST 67 as an internal standard.[19] Despite the rather short data acquisition time, the fitting figures of merit, *i.e.* chi2-Rwp-Rp,[15] indicate that the quality of the data suffices to provide a solid basis for the Rietveld treatment.

In a second stage, kinetic experiments have been performed to study the crystallisation of mullite as a function of time at given temperatures, *i.e.* under isothermal kinetic conditions, using in situ HT-XRPD. The in situ HT-XRPD technique allows one to exploit complementary features with respect to thermal-gravimetry's (TGA): (i) ∼1 g is the sample quantity employed during the HT-XRPD measurements, instead of ∼1–10 mg for TGA; (ii) the sample is heated by an S-type thermocouple, thus minimising the heat and mass transfer effects; (iii) the solid reactants, intermediate and final products can be directly observed by means of their diffraction peaks which bear a wealth of information about the phases in question.

The heating rate used to achieve the chosen temperatures has been set at 25 °C/min for all the measurements, and *T* has been kept fixed for some hours until full completion of the crystallisation reaction. Temperature is kept stable in the isothermal runs by two large alumina fibre blocks, heated by $MoSi_2$ resistances.[13] The highest temperature (1140 °C) among those explored has been fixed so that mullite formation during the first minutes does not exceed 1 wt%. The data collections were performed on the angular range of 39.25–40.25° 2θ, with a 2θ step size of 0.03° and counting time of 2 s/step. Such an experimental set-up allows one (i) to have fast data collections with a satisfactory signal to

noise ratio, and (ii) to monitor as a function of time the rapid changes affecting the intensity of the (1 2 1) peak of mullite.

3.2. Scanning electron microscopy (SEM)

The samples undergone isothermal kinetic runs have then been etched by a solution of 8 M fluoroboric acid for 1 h to remove the amorphous phase. This allows one to obtain specimens suited to high definition morphological images collection, using a scanning electron microscope (SEM) to observe the mullite crystal habit. We have recorded secondary electron (SE) images by means of a Cambridge STEREOSCAN 360 SEM with an acceleration current of 15 kV, a beam size of ~100 nm and a working distance of 11 mm. The image resolution is of 1024 × 730 pixels and 1 pixel corresponds to 1.5 μm.

4. Solid-state kinetic analysis

The kinetics of the mullite crystallisation was followed measuring the integrated intensities of the (1 2 1) Bragg peak that minimises the interferences due to superposition with other signals of quartz, feldspar and instrumental set-up. The (1 2 1) intensity was first normalised with respect to its intensity observed in the sample at full completion of the solid-state reaction involved, and then used to calculate the mullite conversion α-parameter.

We have elected two models[20–22] to describe the mullite formation kinetics: (i) the Avrami model, to extract the reaction order and to have an overview upon the reaction mechanism; (ii) two Avrami–Erofeyev models on the basis of the reference–time analysis, which is here omitted for the sake of brevity. Beneath we recall some basic relationships related to the aforesaid formalisms:

(a) the Avrami model, which results in[20]

$$(kt)^n = -\ln(1-\alpha) \quad (1)$$

where $k = A\exp(-E_a/RT)$; A is the pre-exponential, *i.e.* frequency factor, E_a the apparent activation energy, R the gas constant, and T the absolute temperature;

(b) the Avrami–Erofeyev models, which imply random instant nucleation followed by two- (A2) or three- (A3) dimensional growth of nuclei, and whose equations are shown below

$$kt = (-\ln(1-\alpha))^{1/2} \quad (2)$$

$$kt = (-\ln(1-\alpha))^{1/3}. \quad (3)$$

A2 and A3 are sensitive to the mullite crystal morphology, the former and the latter relying upon a cylindrical (two-dimension model) or spherical (three-dimension model) symmetry of the mullite growth process, respectively.[23]

The interpolation of our data was carried out using the logarithmic form of the equations above, *i.e.*

$$n\ \ln t + n\ \ln k = \ln(-\ln(1-\alpha)) \quad (4)$$

$$\ln k + \ln t = \ln[(-\ln(1-\alpha))^{1/2}] \quad (5)$$

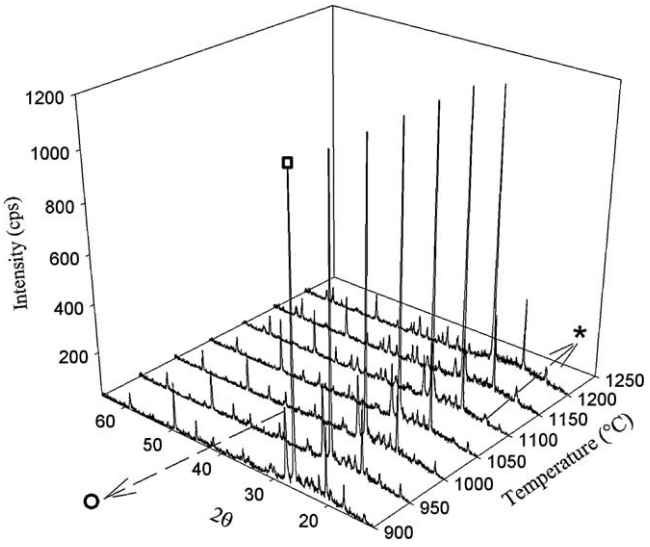

Fig. 1. Diffraction patterns of the spectra collected in the selected temperature range 900–1200 °C, every 50th centigrade (sample *I3*). The symbols: (□), (◯) and (*) refer to the main quartz, feldspar and mullite peaks, respectively.

$$\ln k + \ln t = \ln[(-\ln(1-\alpha))^{1/3}] \quad (6)$$

Eventually, the k values at different temperatures were used to extract the apparent activation energy according to the Arrhenius equation.

5. Results

5.1. HT-XRPD at equilibrium conditions

The HT-XRPD full patterns from *RT* to 1200 °C provide an overview of the reactions taking place in the industrial-like blends on study, in terms of phase occurrence. The sequence of phase transformations upon heating is thoroughly reported in literature[4,23–25] and can be outlined as follows: de-hydroxylation of kaolinite starting in the range of 400–500 °C, followed by the transformation of meta-kaolinite to an Al–Si–spinel structure at $T > \sim 950$ °C (detected only in the sample *I4*) and associated with the growth of a Si-rich amorphous phase as T approaches 1050 °C. The transition of quartz and feldspar[4] (*i.e.* α–β quartz and low-high albite) are also observed. In the temperature range 1100–1150 °C, the intensities of the X-ray reflections of Al–Si–spinel decrease, whereas Bragg peaks related to mullite appear (Fig. 1). Feldspar is visible up to 1150 °C, while above such temperature its Bragg peaks exhibit quickly decreasing intensities. Upon raising temperature towards 1200 °C, the mullite reflections grow sharper and sharper, but gain in intensity (Fig. 1). Above 1200 °C no remarkable change in the X-ray reflections of mullite is observed, which thing hints that either the growth reaction of mullite has achieved completion or it proceeds governed by a very slow kinetics. The XRPD patterns collected at 1200 °C show the presence of quartz, which is the most abundant crystalline phase, together with mullite and a Si-rich glass phase, the latter clearly signalled by a bump in the range 15–30° 2θ (Fig. 1).

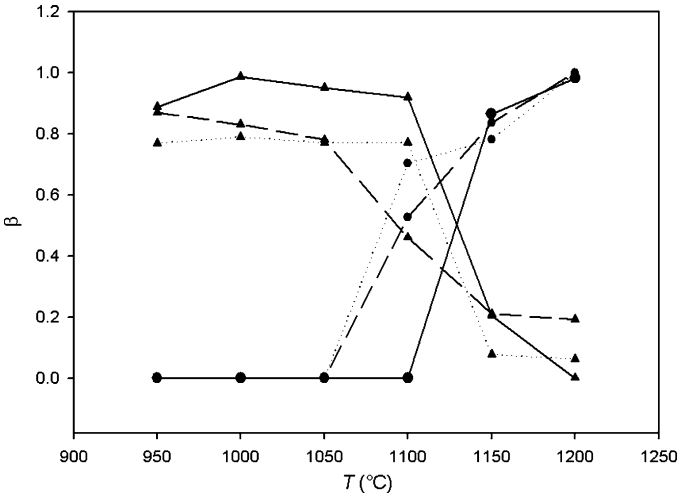

Fig. 2. The β-parameter (see text for its definition) for mullite and feldspars as a function of T. Circles and triangles refer to mullite and feldspar, respectively. *I2*: solid line; *I3*: dashed line; *I4*: dotted line.

The temperature of mullite formation seems to be co-related to the phase composition of the starting blends (Table 1). In particular, in the sample *I2*, which has the lowest content of feldspar (10 wt%), mullite appears at 1150 °C, whereas in the samples *I3* and *I4*, with feldspar amounts of 22 and 40 wt%, respectively, the onset of the mullite crystallisation takes place at a ~50 °C lower temperature. The Al–Si–spinel phase occurs only in the sample *I4* at 1050 °C and is observable up to 1100 °C, where mullite crystallisation starts.

In Fig. 2, the β-parameter (see below) has been calculated for mullite and feldspar as a function of temperature in order to visualise (i) the progress of the reactions involving these two phases and (ii) how they co-relate with one another. In particular β is defined as follows:

$$\beta = \left(\frac{I_o - I_T}{I_o - I_\infty}\right)$$

where I_o, I_T and I_∞ refer to a quantity proportional to the integrated intensity of a chosen peak for each phase measured at room temperature, at T (from 950 to 1200 °C) and at ambient conditions after cooling, respectively. Note that we use for I_X the integrated intensities of the (0 0 2) peak of feldspar and (1 2 1) of mullite, both divided by the (1 0 0) integrated intensity of quartz normalised to the quartz weight content, to account for the diffraction intensity decrease as a function of T. In the samples *I2* and *I3*, β_{mullite} does not show any appreciable change until 1150 and 1100 °C, respectively; then, it starts to increase along with a decrease of β_{feldspar} (particularly in *I3*). Conversely, in the sample *I4*, β_{mullite} exhibits a remarkable increase at 1100 °C, but without involving any appreciable loss of feldspar, which instead takes then place at higher T.

5.2. Isothermal kinetic analysis

We have analysed our data following the method proposed by Hancock and Sharp,[21] which relies on the plot of $\ln(-\ln(1-\alpha))$ versus $\ln t$ (Eq. (4)). Fig. 3 displays three

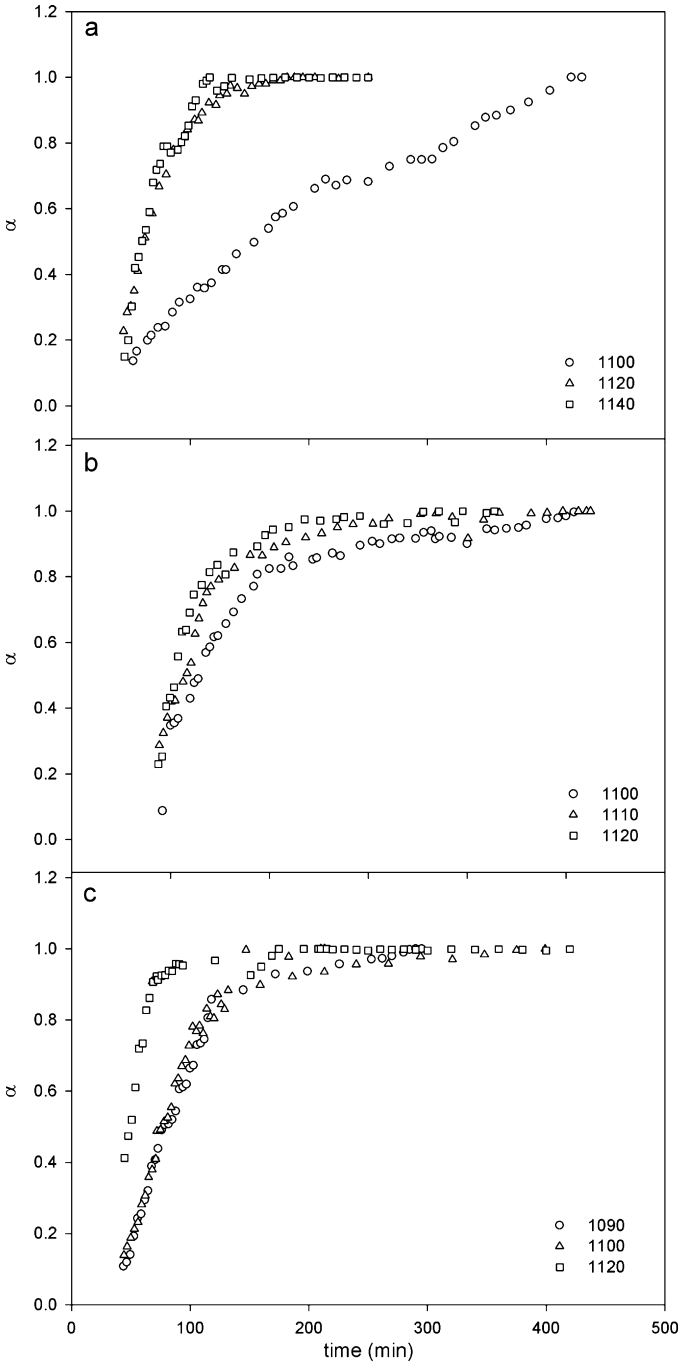

Fig. 3. α-values for the three isothermal runs (°C) as a function of time in (a) *I2* and (b) *I3* and (c) *I4*, respectively.

isothermal α–t curves of mullite crystallisation in the studied samples.

The $\ln(-\ln(1-\alpha))$ trend as a function of $\ln t$ is linear over the conversion range $0.15 < \alpha < 0.5$, as shown in Fig. 4. This hints that mullite crystallises following a mono-step process, which implies one only apparent activation energy value. The slope of the linear function fitted through the points of each isotherm allows one to extract the reaction order value, n, that provides information on the transformation mechanism driving the mullite formation. In Table 2 the values of n for each kinetic isothermal experiment and the related regression coefficients are

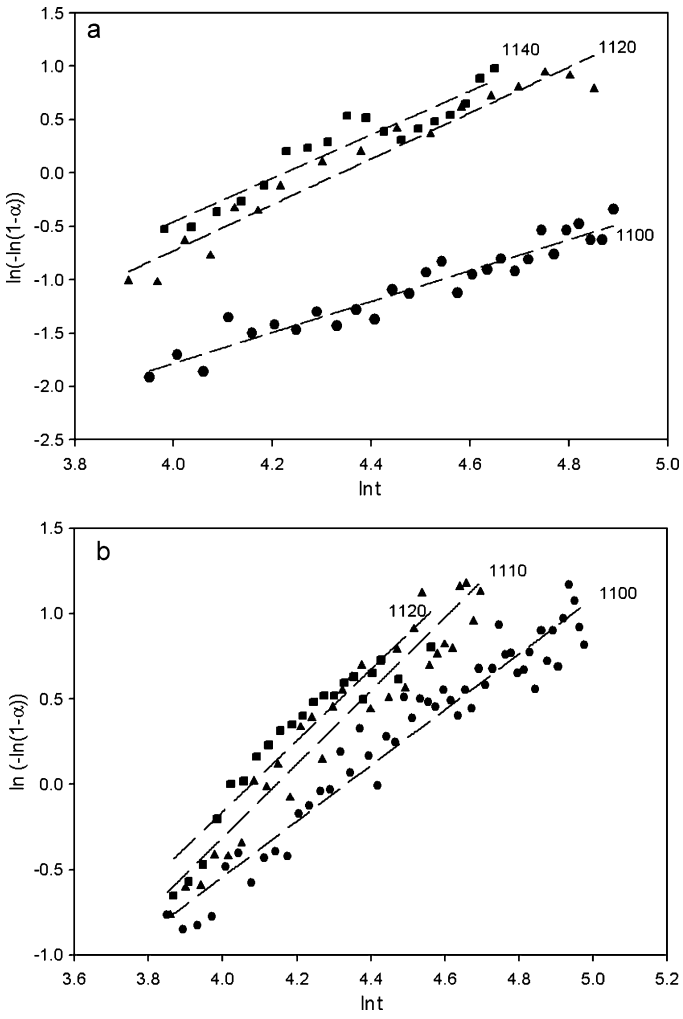

Fig. 4. Plot of $\ln(-\ln(1-\alpha))$ versus $\ln t$ for the isothermal runs (°C) of samples (a) *I2* and (b) *I3*, respectively.

reported: an average value of 1.88 and 1.95 is determined for the sample *I2* and *I3*, respectively, whereas a value as large as 2.76 is observed for the sample *I4*. No correlation between n and temperature is appreciable.

Table 2
Results of the $\ln(-\ln(1-\alpha))$ vs $\ln t$ analysis.

Sample	T (°C)	n	r
I2	1100	1.45	0.92
	1120	2.15	0.97
	1140	2.04	0.96
		1.88 (average)	
I3	1100	1.63	0.90
	1110	2.16	0.93
	1120	2.06	0.91
		1.95 (average)	
I4	1090	2.56	0.98
	1110	2.75	0.98
	1120	2.96	0.98
		2.76 (average)	

Table 3
Rate constants from kinetic analysis.

Sample	Kinetic model	T (°C)	$-\ln k$	r
I2	A2	1100	3.79	0.92
	A2	1120	5.46	0.93
	A2	1140	6.54	0.89
I3	A2	1100	3.26	0.96
	A2	1110	3.56	0.94
	A2	1120	4.33	0.86
I4	A2	1090	5.78	0.98
	A2	1100	6.14	0.98
	A2	1120	6.55	0.98
I4	A3	1090	3.85	0.97
	A3	1100	4.09	0.92
	A3	1120	3.83	0.92

The resulting values of n suggest the physical kinetic model[21] most appropriate to fit our data from the isothermal runs. The isokinetic data belonging to *I2* and *I3* have been interpolated by the kinetic equation A2, whereas for *I4*, both A2 and A3 are suited to fit the experimental data.

Once chosen a kinetic equation, one is allowed to calculate the values of the rate constants k (see Table 3) using the integral form of the general kinetic expression, *i.e.* $kt = f(\alpha)$. Fig. 5 reports the Avrami–Erofeyev model (A2) fitted to our observations, and shows a good agreement between theory and measurements. Table 4 reports the E_a-values obtained from k via the Arrhenius equation (see Fig. 6). The A2 model provides a more consistent description to interpret the kinetic mechanism of mullite formation than A3 does, for all the investigated samples.

A straightforward correlation between the feldspar amount and the value of the E_a is found and displayed by Fig. 7. Note that the highest content of mullite developed at the end of the kinetic isothermal runs is observed in the sample *I4* (∼25 wt%), whereas lower amounts are measured in the samples *I2* and *I3* (∼18 wt%).

Finally, the samples treated at the highest achieved temperatures among isothermal kinetic runs have also been characterised

Table 4
Values of the apparent activation energy obtained from the slope of the Arrehnius plot.

	E_a (kJ/mol)	r
This work		
I2 (kinetic model A2[a])	1111	0.98
I3 (kinetic model A2[a])	628	0.98
I4 (kinetic model A2[a])	394	0.97
I4 (kinetic model A3[a])	115	0.63
Previous studies		
Chen et al.[7]	1182	–
Tkalcec et al.[8]	970[b]	–
Gualtieri et al.[11]	523[c]	–
Gualtieri et al.[11]	360[d]	–
Romero et al.[9]	599	–

[a]The reaction mechanism is described in Hancock and Sharp[20]; [b] refers to the E_a value calculated as an average over three samples; [c] and [d] refer to the E_a values for the sample KGa-1 and KGa-2, respectively.

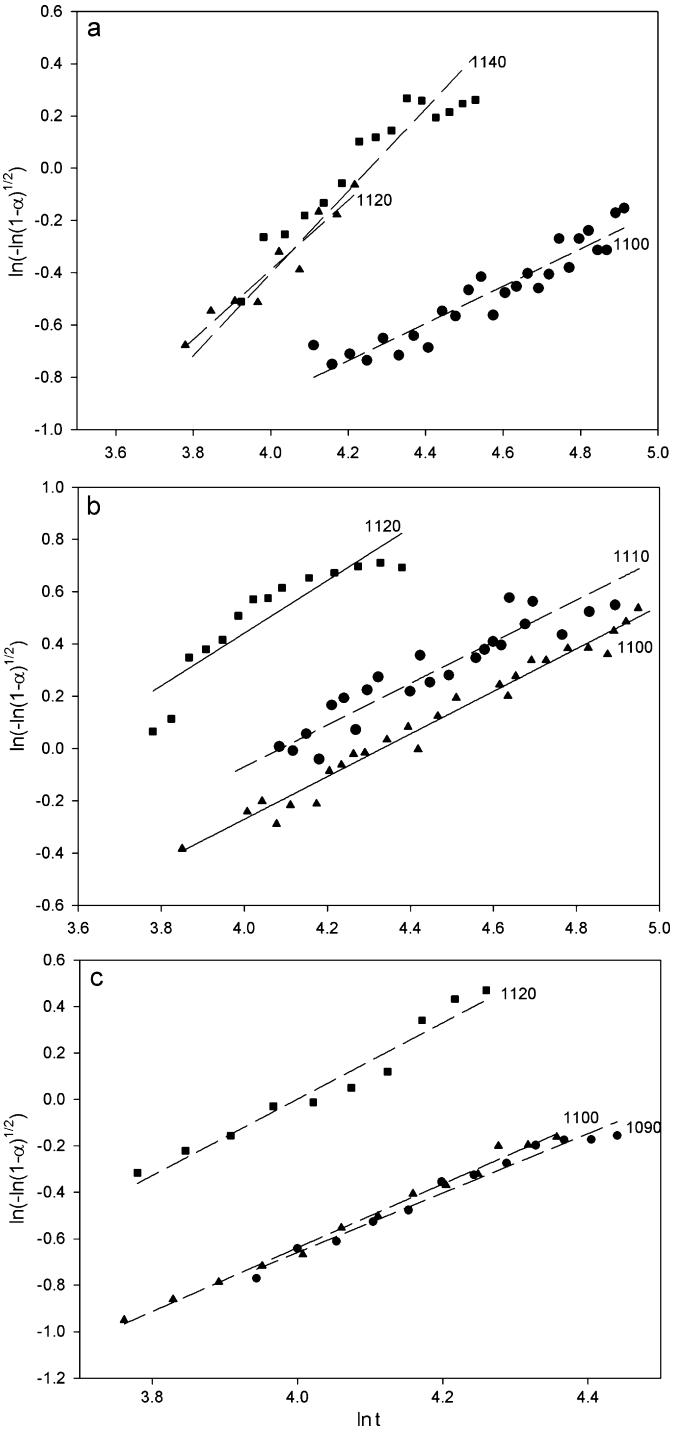

Fig. 5. Plot of $\ln[(-\ln(1-\alpha))^{1/2}]$ versus $\ln t$ for the isothermal runs (°C) of samples (a) *I2* and (b) *I3* and (c) *I4*, respectively.

by SEM (Fig. 8a–d): all the aggregates bear small (about 0.1 μm) almost cubic-like mullite crystals, referred to as "primary mullite", associated with longer (>1 μm) needle-shaped mullite, *i.e.* "secondary mullite", arranged in an interlocking structure. The presence of few prismatic crystals longer than 10 μm is a common feature in all the investigated samples. In *I4* is observable a higher content of "secondary" mullite, whose growth relates to feldspar relicts, than in *I2* and *I3*.

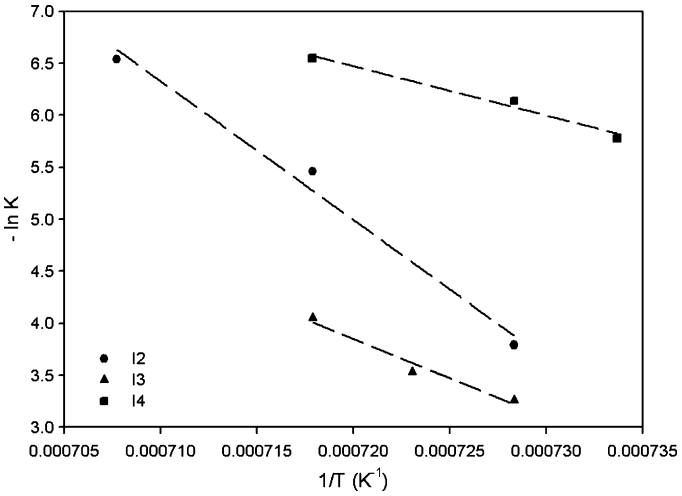

Fig. 6. Arrhenius plot for the investigated samples.

6. Discussion

The mullitisation temperature observed in our samples shows discrepancies with earlier determinations from literature (Table 1). In the present study, the start of mullite growth can be set at 1100 °C in the samples *I3* and *I4*, whereas a higher *T* is required for *I2*, *i.e.* the sample with the lowest feldspar content. In such a light, feldspar plays a role in lowering the *T* of liquid formation (see Carty and Senapati[4]) and the temperature for mullite nucleation and growth, during the firing of a porcelain body.

Gualtieri et al.[11] pointed out that the mullitisation temperature, using kaolin as a starting material, is higher than 1300 °C and similar values are observed when sol–gel techniques are used for the mullite formation.[8] A lower *T* value has been determined if pressed kaolinite powders are used,[7] but the lowest temperature found out is reported by Romero et al.[9] who used as a precursor a chemical mixture similar to sample *I4*. All this implies that the *T* of mullitisation cannot be straightforwardly related to the nature of the starting materials, only. Besides, dif-

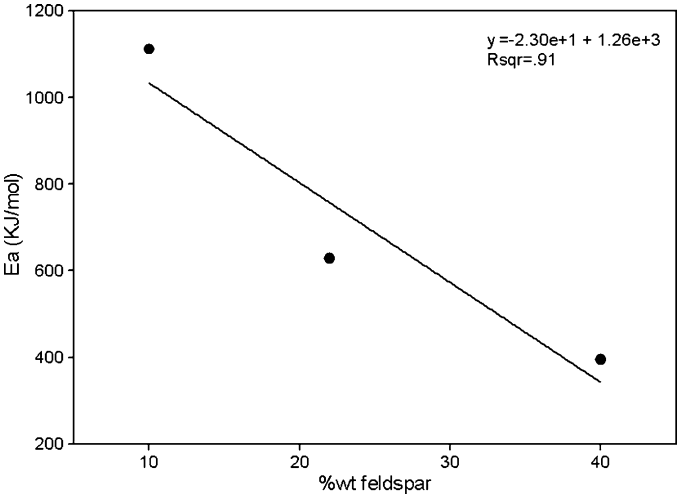

Fig. 7. Relationship between the feldspar amount in the samples with their apparent activation energy (E_a).

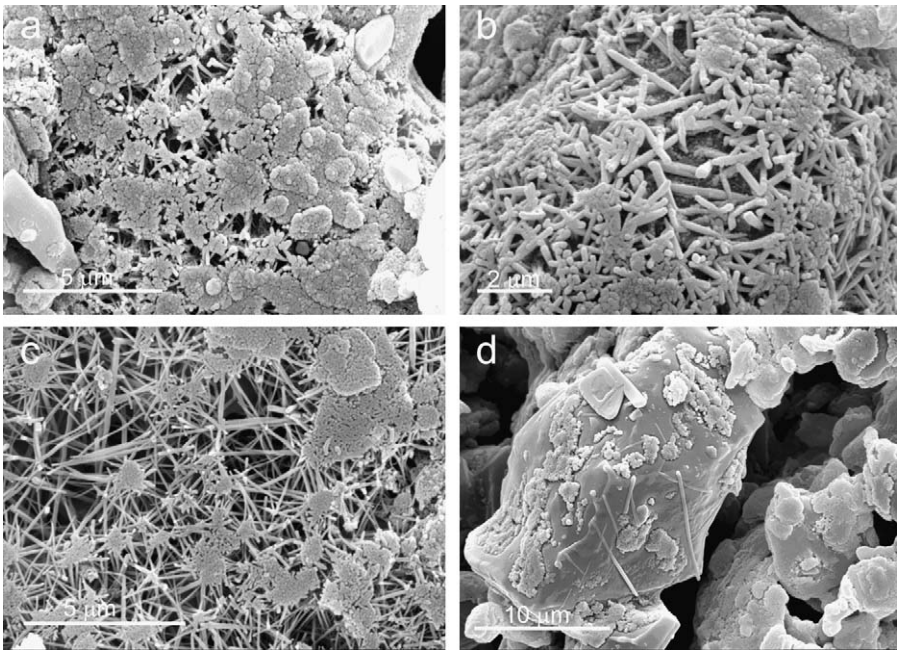

Fig. 8. SEM-images: "primary" and "secondary" mullite with different size and morphology in the samples (a) *I2*, (b) *I3* and (c) *I4*. Note the different contents of the two forms of mullite in the investigated samples; (d) "secondary" mullite crystals growing on feldspar relicts in sample *I4*.

ferences between *T*s of mullitisation arose from the heating rate used as demonstrated by Castelein et al.[27]

Analysing the diffraction patterns recorded at equilibrium conditions, the crystallisation of mullite occurs via a direct route without any spinel intermediate phase in the sample *I2* and *I3*, whereas it is anticipated by the growth of an Al–Si–spinel structure in sample *I4*. Fig. 2 shows that β_{mullite}s in the samples *I2* and *I3* are associated to a decrease of β_{feldspar}. It is known that the "primary" mullite is related to a topotactic growth from metakaolinite[24–26] whereas the "secondary" one seems to be boosted by the additional Al_2O_3 from the dissolution of feldspar. In such a view, it is possible that primary and secondary mullite crystallisation processes start simultaneously, in *I2* and *I3*. Conversely, the sample *I4* suggests a different evolution of the reaction, as the increase of β_{mullite} at 1100 °C is not accompanied by any evidence of a decrease of feldspar's, hinting therefore at an onset of "primary" mullite formation, only. Then, at higher temperature β_{mullite} grows in value, while that of feldspar drops. This is consistent with that the feldspar dissolution promotes the formation of secondary mullite, in keeping with our SEM-observations showing a remarkably higher content of needle-like secondary mullite crystals embedded in a glassy matrix in the feldspar-richest sample *i.e*. *I4*, than in *I2* and *I3* (see Fig. 8). Such aspects are in keeping with that increasing the content of feldspar boosts growth of mullite. Lastly, the Bragg peaks of mullite exhibit a decrease of breadth as a function of *T*, presumably because of a progressive structure regularization and relief of stress.

The analysis of the α–t data and double logarithmic plots, leads to that:

(i) $\ln(-\ln(1-\alpha))$ is well fitted by a linear function in $\ln t$ (Fig. 4), thus suggesting that a single reaction mechanism describes the formation of mullite;
(ii) the A2 model provides a sound description of the reaction, and therefore the transformation on study exhibits a common driving mechanism in all the samples investigated;
(iii) the reaction seems to develop according to a two-dimensional growth of nuclei.

Gualtieri et al.[11] claim that the crystallisation of mullite is described by a reaction mechanism that is intermediate between the phase boundary and diffusion, whereas Chen et al.[7] suppose an instantaneous nucleation followed by a crystal growth controlled by diffusion for the mullite formation (Table 4). Romero et al.[9] report that the mullite synthesis is characterised by bulk nucleation followed by a three-dimensional growth of crystals with polyhedron-like morphology controlled by diffusion from a constant number of nuclei. The discrepancies between all these results show that the starting raw materials (involved phases and related particle size distributions), as well as the heating ramp, deeply affect the mechanisms that govern the mullite nucleation and growth.

The present study yields that the reaction mechanism is basically independent of *T*, as the *n*-value does not change as a function of *T*. Such a result is at variance with those from other studies indicating an increasing importance of the diffusion mechanism at high *T*.[11]

The lowest value of E_a (Table 4) is measured in the sample with the highest content of feldspar, in agreement with Castelein et al.[27] who claim that feldspar, which has a high degree of mixing in terms of Al^{3+} and Si^{4+}, contributes to lower E_a for the mullite crystallisation. The E_as of the samples *I3* and *I4* are consistent with those reported by Chen et al.[7] and Gualtieri et al.,[11] but in disagreement with the ones from Tkalcec et al.[8] The discrepancy on the apparent activation energy value of mullitisation can also be attributable to the different homo-

geneity degree of the precursors, as previously mentioned by Chen et al.[7]

Fig. 7 allows one to visualise the dependence of E_a on the feldspar content. In particular a straightforward correlation between the amount of feldspar in the investigated samples and their E_a values is observed: the larger the content of feldspar, the lower the activation energy of mullitisation ($dE_a/dx_{feldspar} \sim -23(4)$ kJ/mol/wt, where $x_{feldspar}$ is the weight fraction of feldspar). Therefore the different feldspar content in the starting material influences the T of mullitisation and the growth of the mullite, while it seems to be immaterial to the nature of the reaction mechanism which governs the mullite formation.

7. Conclusions

The mullitisation process has been followed by means of HT-XRPD and using as precursors a mixture of kaolin, quartz and feldspar, according to a common industrial practice of the sanitary-ware production. The influence of the phase composition on the mullitisation process has been investigated by changing the quartz (filler) to feldspar (flux) ratio.

The following results have been achieved:

(i) the kinetic of mullitisation here investigated is a one step reaction, fairly well modelled by a random nucleation followed by a two dimension growth of nuclei mechanism;
(ii) the phase composition, in terms of filler to flux ratio, does not seem to affect such mechanism; the T of mullitisation and the E_a value, as well as the amount of primary and secondary mullite formed within the sintered samples, depend on the flux content;
(iii) an increase of the feldspar content lowers the activation energy of mullitisation, resulting in a boost for the mullite growth ($dE_a/dx_{feldspar} \sim -23(4)$ kJ/mol/wt).

References

1. Preston RJ, Dempster TJ, Bell BR, Rogers G. The petrology of mullite-bearing peraluminous xenoliths. Implications for contamination processes in basaltic magmas. *J Petrol* 1999;**40**:549–73.
2. Leonelli C, Bondioli F, Veronesi P, Romagnolo M, Manfredini T, Pellacani GC, et al. Enhancing the mechanical properties of porcelain stoneware tiles: a microstructural approach. *J Eur Ceram Soc* 2001;**21**:785–93.
3. Stathis G, Ekonomakou A, Stournaras CJ, Ftikos C. Effect of firing conditions, filler grain size and quartz content on bending strength and physical properties of sanitaryware porcelain. *J Eur Ceram Soc* 2004;**24**:2357–66.
4. Carty WM, Senapati U. Porcelain – raw materials, processing, phase evolution and mechanical behaviour. *J Am Ceram Soc* 1998;**81**:3–20.
5. Iqbal Y, Lee WEJ. Microstructural evolution in triaxial porcelain. *J Am Ceram Soc* 2000;**83**:3121–7.
6. Chen YF, Wang MC, Hon MH. Kinetics of secondary mullite formation in kaolin–Al_2O_3 ceramics. *Scripta Mater* 2004;**51**:231–5.
7. Chen YF, Wang MC, Hon MH. Phase transformation and growth of mullite in kaolin ceramics. *J Eur Soc Ceram* 2004;**24**:2389–97.
8. Tkalcec E, Ivankovic H, Nass R, Schmidt H. Crystallization kinetics of mullite formation in diphasic gels containing different alumina components. *J Eur Soc Ceram* 2003;**23**:1465–75.
9. Romero M, Martín-Márquez J, Rincón JMA. Kinetic of mullite formation from a porcelain stoneware body for tiles production. *J Eur Soc Ceram* 2006;**26**:1647–52.
10. Lee WE, Souza GP, McConville CJ, Tarvornpanich T, Iqbal Y. Mullite formation in clays and clay-derived vitreous ceramics. *J Eur Soc Ceram* 2008;**28**:465–71.
11. Gualtieri A, Bellotto M, Artioli G, Clark SM. Kinetic of the kaolinite-mullite reaction sequence. Part II: mullite formation. *Phys Chem Miner* 1995;**22**:215–22.
12. Pagani A, Francescon F, Pavese A, Diella V. Sanitary-ware vitreous body characterization method by optical microscopy, elemental maps, image processing and X-ray powder diffraction. *J Eur Soc Ceram* 2010;**30**:1267–75.
13. Dapiaggi M, Artioli G, Petras L. A newly developed high-temperature chamber for in situ X-ray diffraction. Setup and calibration procedures. *Rigaku J* 2002;**19**:35–41.
14. Young RA. *The Rietveld method*. Oxford: University Press; 1993.
15. McCuster LB, Von Dreele RB, Cox DE, Louër D, Scardi P. Rietveld refinement guidelines. *J Appl Crystallogr* 1999;**32**:36–50.
16. Madsen IC, Scarlett NVY, Granswick LMD, Lwin T. Outcomes of the international union of crystallography commission on powder diffraction round robin on quantitative phase analysis: sample 1a to 1 h. *J Appl Crystallogr* 2001;**34**:409–26.
17. Larson AC, Von Dreele RB. *General Structure analysis system (GSAS)*. LAUR Rep. 86-748, Los Alamos Natl Lab, Los Alamos; 1986.
18. Toby BH. EXPGUI, a graphical user interface for GSAS. *J Appl Crystallogr* 2001;**34**:210–3.
19. Gualtieri AF. Accuracy of XRPD QPA using the combined Rietveld-RIR method. *J Appl Crystallogr* 2000;**33**:267–78.
20. Garner WE, editor. *Chemistry of the solid state*. New York: Academic Press; 1955.
21. Hancock JD, Sharp JH. Method of comparing solid-state kinetic data and its application of kaolinite, brucite, and $BaCO_3$. *J Am Ceram Soc* 1972;**55**:74–7.
22. Brown ME, Dollimore D, Galwey AK. Theory of solid state reaction kinetics. In: Bamford CH, Tipper CFH, editors. *Comprehensive chemical kinetics*, vol. 22. Amsterdam: Elsevier; 1980. p. 41–113.
23. Khawam A, Flanagan DR. Solid-state kinetic models: basics and mathematical fundamentals. *J Phys Chem* 2006;**110**:17315–28.
24. Brindley GW, Nakahira M. The kaolinite-mullite reaction series: I. A survey of outstanding problems. *J Am Ceram Soc* 1959;**42**:311–4.
25. Brindley GW, Nakahira M. The kaolinite-mullite reaction series: II. Metakaolin. *J Am Ceram Soc* 1959;**42**:315–8.
26. Brindley GW, Nakahira M. The kaolinite-mullite reaction series: III. The high temperature phases. *J Am Ceram Soc* 1959;**42**:319–24.
27. Castelein O, Guinebretiere R, Bonnet JP, Blanchard P. Shape, size and composition of mullite nanocrystals from a rapidly sintered kaolin. *J Eur Soc Ceram* 2001;**21**:2369–76.